Biochemistry

pubs.acs.org/biochemistry Article

Accumulation and Pulse Electron Paramagnetic Resonance Spectroscopic Investigation of the 4-Oxidobenzyl Radical Generated in the Radical *S*-Adenosyl-L-methionine Enzyme HydG

Guodong Rao, Nanhao Chen, David A. Marchiori, Lee-Ping Wang, and R. David Britt*

Cite This: *Biochemistry* 2022, 61, 107−116 Read Online

ACCESS | Metrics & More | Article Recommendations | Supporting Information

ABSTRACT: The radical *S*-adenosyl-L-methionine (SAM) enzyme HydG cleaves tyrosine to generate CO and CN^- ligands of the [FeFe] hydrogenase H-cluster, accompanied by the formation of a 4-oxidobenzyl radical (4-OB•), which is the precursor to the HydG *p*-cresol byproduct. Native HydG only generates a small amount of 4-OB•, limiting detailed electron paramagnetic resonance (EPR) spectral characterization beyond our initial EPR lineshape study employing various tyrosine isotopologues. Here, we show that the concentration of trapped 4-OB• is significantly increased in reactions using HydG variants, in which the "dangler Fe" to which CO and CN^- bind is missing or substituted by a redox-inert Zn^{2+} ion. This allows for the detailed characterization of 4-OB• using high-field EPR and electron nuclear double resonance spectroscopy to extract its *g*-values and $^1H/^{13}C$ hyperfine couplings. These results are compared to density functional theory-predicted values of several 4-OB• models with different sizes and protonation states, with a best fit to the deprotonated radical anion configuration of 4-OB•. Overall, our results depict a clearer electronic structure of the transient 4-OB• radical and provide new insights into the radical SAM chemistry of HydG.

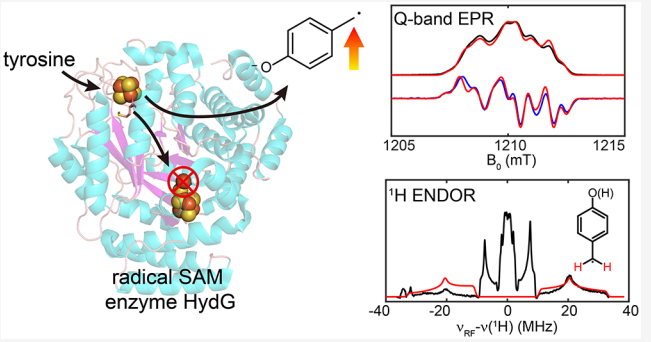

INTRODUCTION

Enzymatic reactions involving radical intermediates are widely present in metabolic and biosynthetic pathways. These radical intermediates can perform unusual and difficult biochemical reactions, oftentimes involving H-atom abstraction from inert X−H bonds. Over the last 20 years, the radical *S*-adenosyl-L-methionine (rSAM) family of enzymes has emerged, which generate an active 5′-dAdo radical upon one-electron reduction of SAM bound to a [4Fe−4S] cluster.[1,2] This long sought and elusive 5′-dAdo radical and the associated Fe−S cluster-bound organometallic species, **Ω**, have recently been trapped and characterized in a wide range of rSAM enzyme systems,[3−7] reinforcing the paradigm of rSAM enzyme catalysis while providing new insights into the mechanistic details. In most rSAM enzymes, the 5′-dAdo radical activates the substrate by H-atom abstraction, leading to the formation of a substrate-related organic radical, as detected in a number of rSAM enzymes involved in amino acid metabolism and natural product biosynthesis.[8−13] Research on these systems has greatly advanced our understanding of radical enzyme catalysis and provides a foundation for future application of engineered rSAM enzymes as biocatalysts.[2]

HydG, an extensively studied member of the rSAM enzyme superfamily, carries out the first step in the biosynthesis of the active-site H-cluster of the [FeFe] hydrogenase, a complex Fe−S enzyme of great interest in cellular metabolism and renewable energy.[14−18] Studies on HydG from various organisms have demonstrated that it is a bifunctional enzyme that harbors two Fe−S clusters (Figure 1A) with two distinct roles: (1) radical cleavage of its substrate Tyr leading to the formation of CO and CN^- and (2) then forming an $[Fe(cysteinate)(CO)_2(CN)]^-$ organometallic "synthon" product. This organometallic complex is the substrate for the next radical SAM enzyme HydE, which we propose converts two of these $[Fe(cysteinate)(CO)_2(CN)]^-$ moieties into a dimeric $[Fe_2S_2(CO)_4(CN)_2]$ precursor to the final H-cluster.[8,19−23]

In more detail, rSAM chemistry is initiated at the $[4Fe−4S]_{RS}$ cluster bound in the N-terminus of HydG, and the 5′-dAdo radical abstracts the amino hydrogen from Tyr, which induces a homolytic Cα−Cβ cleavage (Figure 1B). This bond cleavage leads to the formation of 4-OB•, along with a dehydroglycine (DHG) fragment, which is then converted into CO and CN. Our recent quantum computational study

Received: September 17, 2021
Revised: December 17, 2021
Published: January 6, 2022

https://doi.org/10.1021/acs.biochem.1c00619
Biochemistry 2022, 61, 107−116

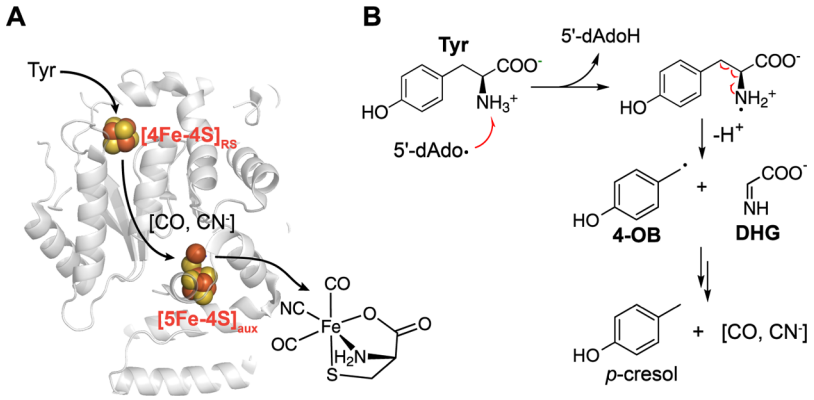

Figure 1. Structure and function of HydG. (A) Tyr is processed at the two Fe−S clusters sequentially to form the organometallic product. (B) rSAM chemistry occurring at the N-terminal $[4Fe{-}4S]_{RS}$ cluster.

proposes that once formed, 4-OB$^{\bullet}$ abstracts an H atom from the nitrogen of DHG, which fragments into HCN and a $COO^{-\bullet}$ radical, with the latter converted to CO via a redox reaction at the "dangler" Fe site of the $[5Fe{-}4S]_{aux}$ cluster (Figure 1).[24] A second equivalent of the abovementioned steps leads to the formation and release of the [Fe(cysteinate)-$(CO)_2(CN)$] product of HydG.[25−27]

Interestingly, studies on the rSAM chemistry of HydG have demonstrated that a variety of radical intermediate species may be generated depending on reaction conditions, showcasing the rich chemistry that HydG may perform. In the native reaction pathway, a small amount of 4-OB$^{\bullet}$ is observed and is maximized approximately 2 s after reaction initiation (∼3 μM).[8] The decay of 4-OB$^{\bullet}$ at prolonged reaction time is accompanied by the formation of the paramagnetic [4Fe−4S]−[Fe(cysteinate)(CO)(CN)] species (complex A), which has been characterized by electron paramagnetic resonance (EPR) spectroscopy.[25] HydG has been used as a conduit to study the elusive 5′-dAdo radical. Sayler and co-workers were able to trap and characterize the 5′-dAdo radical in HydG using the substrate analogue *cis-p*-coumarate.[6] The sp^2 C−H bonds in *cis-p*-coumarate have a higher bond dissociation energy than native tyrosine, effectively stopping the H atom abstraction process by the 5′-dAdo radical and thereby trapping it for characterization. The Broderick and Hoffmann groups have together utilized cryogenic photolysis as a means for studying rSAM chemistry and trapping and characterizing a number of radical species including the 5′-dAdo radical.[4,5,7] In HydG, such experiments have found that SAM or its ethyl analogue SEM undergoes alternative S−C homolytic bond cleavage to generate methyl or ethyl radicals.[28,29]

Despite these discoveries, our understanding of 4-OB$^{\bullet}$ and its role in HydG catalysis is incomplete. The low concentration of 4-OB$^{\bullet}$ generated in previous studies has thus far limited its detailed characterization. Although our QM/MM studies have suggested that 4-OB$^{\bullet}$ could react with DHG to generate CN^- and a carbon dioxide radical anion ($COO^{-\bullet}$), experimental results reinforcing this computational proposal are lacking. It was shown that when the C-terminal auxiliary Fe−S cluster or the dangler Fe was compromised by mutagenesis (*vide infra*), CO generation was abolished and the rate for CN^- formation was significantly decreased.[8,30] These results indicate that the reactions of CO/CN formation in HydG can be significantly affected when the auxiliary cluster is modified, but the formation of the associated radical intermediates in these scenarios has yet to be investigated in more detail. In addition, 4-OB$^{\bullet}$ is also the proposed intermediate in ThiH, a HydG homologue used for the synthesis of the thiazole ring of thiamine phosphate,[31] and in the glycyl radical enzyme *p*-hydroxyphenylacetate decarboxylase (HpdB).[32,33] Insights into 4-OB$^{\bullet}$ obtained from HydG thus help deepen our understanding of the reaction mechanisms in these enzymes and radical enzyme catalysis overall.

Here, we report that the removal of the dangler Fe atom in HydG leads to the enhanced accumulation of 4-OB$^{\bullet}$, which provides new opportunities to address fundamental questions in HydG rSAM chemistry.[34] With enhanced signal intensity, we can now perform a detailed EPR and electron nuclear double resonance (ENDOR) characterization of this 4-OB$^{\bullet}$ species, including the determination of its *g*-values and ^{1}H and ^{13}C hyperfine parameters. In addition, although previous work has established the electronic structure of 4-OB$^{\bullet}$ as having major spin density on the benzyl carbon, the question remains regarding the protonation state of the phenolic hydroxyl group.[8] In the current work, our high-resolution EPR and ENDOR data, combined with density functional theory (DFT) calculations of different 4-OB$^{\bullet}$ models, favor a deprotonated radical anion form of this radical situated in the hydrogen bonding network of the protein pocket.

EXPERIMENTAL DETAILS

General. Isotopically labeled tyrosines were purchased from Cambridge Isotope Laboratories, Inc., MA. Protein purification and EPR sample preparation were performed in an anaerobic Coy box (Coy Laboratory Products, Inc., MI) with an H_2 concentration of > 2% and O_2 concentration of < 5 ppm.

EPR Sample Preparation. Strep-II-tagged *Shewanella oneidensis* HydG (UniPort) was recombinantly expressed in the *Escherichia coli* DE3 Δ*iscR* strain and purified using a Strep-column as previously described.[25] The dangler Fe of HydG was removed by incubation with EDTA followed by buffer exchange as previously described.[26] Briefly, to 50 μL of 300 μM HydG solution (50 mM HEPES, 100 mM KCl, pH = 8.0) was added 3 mM SAM, 3 mM dithionite, and 300 μM EDTA. The solution was diluted by 10-fold using the buffer and then concentrated back to the original volume using a 30 kDa-cutoff Amicon centrifugal filter (12 000 rpm for 4 min). $HydG^{Zn}$ was prepared by adding 2 equiv of Zn^{2+} to the dangler Fe-free HydG. To generate the 4-OB$^{\bullet}$-harboring EPR samples, a 50 μL mixture of 300 μM HydG, 2 mM SAM, and 5 mM dithionite was mixed with 10 μL of 10 mM tyrosine (labeled as desired) and transferred into a Ka-band quartz EPR tube. The

https://doi.org/10.1021/acs.biochem.1c00619
Biochemistry 2022, 61, 107−116

reaction mixture was freeze-quenched at 15 s using LN_2. For D-band EPR samples, the reaction mixture was prepared on a glass slide and wicked into D-band capillary quartz tubes.

EPR Spectroscopy. EPR spectroscopy was performed in the CalEPR center in the Department of Chemistry at the University of California, Davis. Continuous-wave (CW) EPR spectra were recorded on a Bruker Biospin EleXsys E500 spectrometer with a superhigh-Q resonator (ER4122SHQE), together with an ESR900 liquid helium cryostat with a temperature controller (Oxford Instrument ITC503) and gas flow controller. Spectrometer settings were as follows: frequency = 9.39 GHz, conversion time = 40 ms, modulation amplitude = 0.5 mT, and modulation frequency = 100 kHz. Pulsed Q-band ENDOR experiments were performed on a Bruker Biospin EleXsys 580 spectrometer equipped with an R.A. Isaacson cylindrical TE011 resonator.[35] Pulse D-band studies were performed on a home-built 130 GHz spectrometer[36] equipped with a TE_{011}-mode cylindrical resonant cavity designed and manufactured by HF EPR Instruments, Inc (V. Krymov, New York), an 8 T cryogen-free magnet (Cryogenic Limited, UK), an Oxford-CF935 LHe cryostat, and an ITC-503 temperature controller. Spectrometer control is achieved using SpecMan software.[37] The magnetic field for the D-band field-swept spectrum was calibrated using MgO with an Mn^{2+} impurity (95+% fused MgO, Aldrich) with a g-value of 2.00100(5) and a ^{55}Mn hyperfine coupling constant of −243.6(5) MHz, as determined previously.[38,39] The following pulse sequences were employed: electron spin-echo-detected field-swept EPR ($\pi/2-\tau-\pi-\tau-$echo) and Davies ENDOR ($\pi-$RF$-\pi/2-\tau-\pi-\tau-$echo). Spectral simulations were performed in Matlab 2018a with the EasySpin 5.2.28 toolbox.[40]

For nuclei with nuclear spin $I = 1/2$ (^1H and ^{13}C in this study), the ENDOR transitions for the $m_s = \pm 1/2$ electron manifold are observed at the frequencies $\nu_\pm = |\nu_N \pm A/2|$, where ν_N is the nuclear Larmor frequency and A is the field-dependent hyperfine coupling. In the weak coupling case ($A < 2\nu_N$), the two ENDOR branches are centered at ν_N and separated by A. For nuclei with $I > 1/2$ (^2H in this study; $I = 1$), the two ENDOR branches are further split by the nuclear quadrupole interaction (NQI, P), giving ENDOR peaks at $\nu_{\pm,m_I} = |\nu_N \pm A/2 \pm (3P/2)(2m_I - 1)|$. In the case of ^2H, P is usually small compared to A, and the splitting is oftentimes not observed, although the ENDOR lineshape could be affected the small NQI. Occasionally, if $|A|$ is close to $2\nu_N$ (cancellation limit), the low-frequency ENDOR branch is close to zero. In this scenario, this ENDOR branch usually cannot be detected since the RF coil has low response at low frequencies.

The intensity of Davies ENDOR response is modulated by a factor determined by the hyperfine coupling (A, in MHz) and the length of the first inversion π-pulse (t_p, in μs). This factor can be written as:[41]

$$\mathrm{ENDOR}(A, t_p) \propto \frac{1.4(At_p)}{(At_p)^2 + 0.7^2} \quad (1)$$

such that as $A \to 0$, the ENDOR signal vanishes. The lineshape of Davies ENDOR spectra can be significantly distorted, especially when A is small. This modulation factor is taken into consideration in the simulation of some of the ENDOR spectra in this work in order to more accurately reproduce the experimental ENDOR spectra (see the Supporting Information for a script). In addition, for this reason, small hyperfine couplings ($A < 3$ MHz) are usually measured using the complementary Mims ENDOR technique, which is much more sensitive to smaller A values.[42]

Computational Details. The crystal structure 4WCX[20] was obtained from the Protein Databank, and missing residues were modeled manually. The tyrosine ligand position was modeled according to the tryptophan ligand position in the experimental crystal structure of the tryptophan lyase NosL (PDB ID: 4R34[43]). Before the QM/MM simulations, molecular mechanics−molecular dynamics (MM/MD) simulations were carried out to obtain an appropriate equilibrium structure. In MM/MD, the AMBER-FB15 force field[44] and TIP3P-FB model[44] were used for the protein and solvent molecules, respectively, and both of the [4Fe−4S] and [5Fe−5S] clusters were described using Fe−S cluster-specific parameters.[45] In the MM/MD simulations, an added harmonic restraint force with a force constant of 50 kcal/mol/Å^2 was added to maintain the coordination environment of the Fe−S clusters. The SHAKE[46] algorithm was applied to constrain the covalent bond lengths involving hydrogen. The following steps were used to heat up and equilibrate the system gradually: energy minimization followed by a 200 ps heating process in the *NVT* ensemble in which the temperature was gradually ramped up to 300 K. A 200 ps MD simulation was carried out in the *NPT* ensemble to equilibrate the volume of the simulation box. Finally, a 50 ns MD simulation in the *NVT* ensemble was carried out and the final structure was used as the initial structure of the QM/MM simulations.

QM/MM Simulations. The Q-Chem[47] and AMBER[48,49] software packages were applied to do the QM/MM simulations. In the simulations, the QM region was the first chosen as the SAM cofactor, the canonical [4Fe−4S] cluster, and the tyrosine ligand to simulate the SAM decomposition and the radical transfer to the tyrosine ligand. In later reaction steps that did not involve the SAM cofactor and the canonical Fe−S cluster, only the tyrosine ligand, the side chain of the Arg303, and the side chain of the Glu57 were included in the QM region to conserve computational resources. The QM region was described using the B3LYP density functional with the 6-31G* basis set for non-metal atoms and the LANL2DZ basis set/effective core potential combination for the Fe atoms. All the non-QM atoms were treated by the force field with 12 Å cutoff for non-bonded interactions.

EPR Parameters. The DFT calculations of EPR parameters were carried out using ORCA 5.0.2.[50] The initial coordinates of different 4-OB$^\bullet$ models were extracted from the structure models generated as mentioned above and used without further optimization. Single-point energy calculations were carried out using the B3LYP density functional and the def2-TZVP basis set in conjunction with the RIJCOSX approximation for two-electron integrals and the def2/J auxiliary basis set for all atoms.[51−54] EPR calculations were performed using the TPSSH density functional and the EPR-II basis set with the RIJCOSX approximation and the def2/J auxiliary basis set for all atoms.[55] The electrostatic effect of the protein environment was crudely modeled using the conductor-like polarizable continuum model (CPCM)[56] with a dielectric constant of $\varepsilon = 4.0$.[33] An empirical dispersion correction was included in all calculations using the D3BJ keyword in ORCA.[57]

The effect of basis sets on computational results is shown in Table S1. Three basis sets for EPR parameter calculations, EPR-II,[58] IGLO-II,[59] and aug-cc-pVTZ-J,[60] all listed in the manual of ORCA 5.0.2, were employed. EPR-II and IGLO-II

https://doi.org/10.1021/acs.biochem.1c00619
Biochemistry 2022, 61, 107−116

gave very similar results, quite close to experimental data, while aug-cc-pVTZ-J gave overestimated spin−orbit couplings. In the current study, EPR-II appeared to be a good choice of basis sets.

Calculation of pK_a. The pK_a calculations of all the molecules were done using the Terachem software package.[61] Geometry optimizations and vibrational analyses were done using unrestricted B3LYP with the def-TZVP basis set.[62] At the optimized geometry, a single-point energy calculation was performed with the larger def2-TZVP basis set with *f* functions removed, and the free energy difference between the two protonation states was computed as $\Delta G \sim \Delta E$(B3LYP/def2-TZVP-f) + ΔG_{corr}(B3LYP/def-TZVP). To compute the pK_a, the ΔG of the reaction (HA → A^- + H^+) was computed by adding −11.803 eV to the base side of the reaction, corresponding to the standard free energy of a proton in solution.[63] The pK_a was then computed as pK_a = ΔG(HA → A^- + H^+)/2.303 *RT*, where *R* is the gas constant and *T* was set to 298.15 K. In the calculation, the COSMO PCM implicit solvent model was selected with a dielectric constant of 78.3 (that of water).[64]

RESULTS AND DISCUSSION

HydG mutants with the auxiliary Fe−S cluster knocked out (C380S/C383S, with both Cys being ligands to the [5Fe−4S]$_{aux}$ cluster) or the dangler Fe site compromised (H265N, with H265 being an axial ligand to the dangler Fe^{2+}) were investigated for their catalytic activity.[30] Here, we removed the dangler Fe using stoichiometric EDTA followed by buffer exchange without disturbing the protein backbone, a procedure we applied in several previous studies.[26] This approach also allowed us to conveniently place different metal ions, such as Ni^{2+}, Co^{2+}, or Zn^{2+}, in the dangler Fe site, while the peptide backbone of HydG remains intact.[65] As shown in Figure 2, the dangler Fe-removed variant (HydG$^{\Delta Fe}$) and the Zn-substituted variant (HydG^{Zn}) both contain two *S* = 1/2 EPR signals in the $g \sim 2$ region (black traces). The EPR species with g_1 = 2.01 in both cases corresponds to the [4Fe−4S]$_{RS}$−[SAM] species as noted in HydG and other rSAM enzymes,[26] whereas the EPR species with g_1 = 2.06 in the case of HydG$^{\Delta Fe}$ corresponds to [4Fe−4S]$_{aux}$−[cysteinate] and the EPR species with g_1 = 2.07 in the case of HydG^{Zn} corresponds to [4Fe−4S]$_{aux}$−[Zn(cysteinate)] (Figure S1). The *S* = 5/2 EPR signal for the native HydG auxiliary cluster ([4Fe−4S]$_{aux}$−[Fe(cysteinate)]) is not present in both samples, supporting complete removal of the dangler Fe.

The reaction mixtures of both variants, which contain HydG, SAM, Tyr, and dithionite, were freeze-quenched at 15 s after reaction initiation and then examined by EPR. Interestingly, both reaction mixtures contain substantial amounts of organic radical at g = 2.004 (blue and purple traces), corresponding to the previously assigned 4-OB$^\bullet$ in wild-type HydG. Simulations of the spectra obtained at 10 K reveal four *S* = 1/2 EPR species in the $g \sim 2$ region in the sample of HydG^{Zn}: [4Fe−4S]$_{RS}$−[SAM], [4Fe−4S]$_{aux}$−[Zn(cysteinate)], a previously identified unknown [4Fe−4S]$_{RS}$ species, and 4-OB$^\bullet$ (Figure 2). The concentration of 4-OB$^\bullet$ is estimated to be ∼10 μM from spectral simulation (Figure S2), which is ∼10 times higher than that of the wild-type HydG reaction sample prepared under the same reaction conditions and still ∼3 times higher than the maximum 4-OB$^\bullet$ concentration produced in wild-type HydG (at 2 s reaction time). Although the EPR spectra of the reaction mixtures

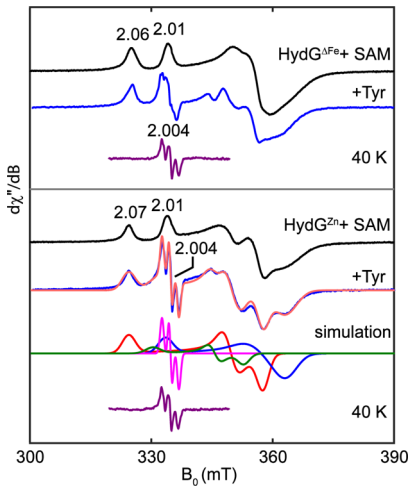

Figure 2. X-band EPR spectra of HydG reaction mixtures freeze-quenched at 15 s. Conditions: 10 K, 0.1 mW (black trace); 10 K, 0.002 mW (blue traces, normalized); and 40 K, 0.02 mW (purple traces). 4-OB$^\bullet$ is labeled as g = 2.004; [4Fe−4S]$_{aux}$−[cysteinate] is labeled as g = 2.06; [4Fe−4S]$_{aux}$−[Zn(cysteinate)] is labeled as g = 2.07; and [4Fe−4S]$_{RS}$−[SAM] is labeled as g = 2.06; see text for details. At 40 K, all signals of the [Fe−S] species relax too fast to be observed, and only the EPR signal corresponding to 4-OB$^\bullet$ is recorded. The reaction mixture can be simulated with four *S* = 1/2 species: red, [4Fe−4S]$_{aux}$−[Zn(cysteinate)]; magenta, 4-OB$^\bullet$; blue, [4Fe−4S]$_{RS}$−SAM; and green, unknown [4Fe−4S]$_{RS}$ species. See Figures S1 and S2 for simulation details and the estimation of 4-OB$^\bullet$ concentration.

generated from HydG$^{\Delta Fe}$ and HydG^{Zn} are slightly different at 10 K, probably due to the slight differences in the EPR features arising from [4Fe−4S] species, the EPR signals corresponding to 4-OB$^\bullet$ have nearly the same lineshape and intensity at 40 K, where all signals corresponding to 4Fe−4S clusters are gone, indicating that they have the same perturbation to the HydG reaction. Indeed, the 4-OB$^\bullet$ signals from both samples also have the same spectral features in pulse EPR and ENDOR experiments. Spectra shown in the following text are obtained from the samples made from HydG$^{\Delta Fe}$, but they are equally applicable to those made from HydG^{Zn}.

The generation and accumulation of 4-OB$^\bullet$ were further confirmed by pulse Q-band echo-detected EPR spectra, which reveal the characteristic 4-OB$^\bullet$ EPR lineshape identical to that obtained from previous Q-band CW EPR measurements (Figure 3A).[8] At higher temperatures (25 K), the electron spin-echo envelope is dominated by the 4-OB$^\bullet$ signal (Figure S3), allowing detailed EPR and ENDOR characterization of 4-OB$^\bullet$ (*vide infra*).

The fact that 4-OB$^\bullet$ is accumulated in the absence of the dangler Fe (or with Fe replaced by Zn) supports the proposal that 4-OB$^\bullet$ is involved in the on-path decomposition of dehydroglycine into CO and CN^- instead of being quenched by the protein environment independently. This observation is consistent with our recent QM/MM study, which suggested a radical relay mechanism from 5′-dAdo to 4-OB$^\bullet$ to the dehydroglycine radical to $COO^{-\bullet}$, with the final formation of the Fe−CO bond on the dangler Fe site.[24] The reaction between 4-OB$^\bullet$ and DHG to generate cyanide and $COO^{-\bullet}$ is calculated to be thermodynamically neutral,[24] and thus, an equilibrium could form. It is therefore reasonable to argue that the absence of the dangler Fe eliminates the driving force of this radical relay, such that the most stable radical on the

https://doi.org/10.1021/acs.biochem.1c00619
Biochemistry 2022, 61, 107−116

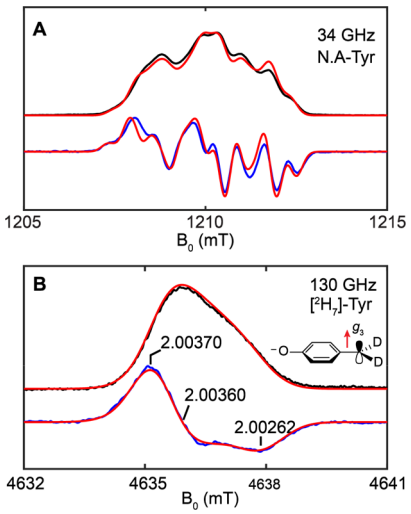

Figure 3. (A) Pulse Q-band echo-detected EPR spectrum of 4-OB• generated from natural abundance Tyr. (B) Pulse D-band echo-detected EPR spectrum of 4-OB• generated from [$^2H_7$]-Tyr in D_2O buffer. Black traces: field-swept spectra. Blue traces: pseudomodulated spectra. Red traces: spectral simulations. Simulation of Q-band spectra: g = [2.00370, 2.00360, 2.00262], HStrain = 12 MHz, two ^1H with A = [65.9, 20.0, 40.7] MHz, and two ^1H with A = [18.2, 7.0, 14.9] MHz (panel A). Simulation of D-band spectra: g = [2.00370, 2.00360, 2.00262], HStrain = [0, 56, 35] MHz, two ^2H with A = [10.1, 3.1, 6.3] MHz, and two ^2H with A = [2.8, 1.1, 2.3] MHz (panel B). Conditions: (A) temperature = 25 K, $\pi/2$ = 12 ns, τ = 300 ns, modulation amplitude = 0.1 mT; and (B) temperature = 25 K, $\pi/2$ = 40 ns, τ = 300 ns, and modulation amplitude = 0.5 mT.

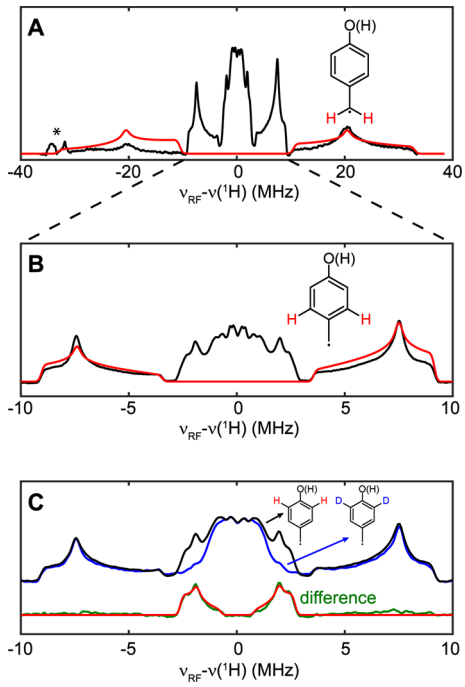

Figure 4. Q-band Davies ^1H ENDOR spectra of differently labeled 4-OB•. Black and blue traces are experimental data and red traces are simulations with ^1H hyperfine couplings of (A) A ^1H = [66, 20, 41] MHz; (B) A ^1H = [18.2, 7.0, 14.9] MHz; and (C) A ^1H = [5.3, 1.5, 3.8] MHz. Conditions: frequency = 34 GHz, temperature = 25 K, inversion pulse = 80 ns, and τ = 300 ns. The asterisk feature in (A) is the third-order harmonics of the ^1H ENDOR response in the central region.

pathway, 4-OB•, owing to its aromaticity, is accumulated at a local energy minimum.

The ready accumulation of 4-OB• allows us to characterize this radical in more detail using a combination of isotopically labeled Tyr substrate and high-resolution EPR spectroscopy. The g-tensor of 4-OB• has not been previously resolved in X-band or Q-band measurements due to its very small g-anisotropy. Using [$^2H_7$]-Tyr as the substrate and a D_2O reaction buffer to minimize the hyperfine broadening of the EPR spectrum, we were able to measure the g-tensor of 4-OB• on a pulse 130 GHz (D-band) spectrometer as g = [2.00370, 2.00360, 2.00262] (Figure 3B), which is only marginally resolved even at this frequency. The g_3 value is fairly close to the free electron g value (2.0023), consistent with 4-OB• being a p_z-type radical and g_3 (g_z) pointing perpendicular to the aromatic plane.

To understand the complex lineshape of the Q-band EPR spectrum arising from multiple overlapping ^1H hyperfine couplings, it is necessary to extract the hyperfine parameters of individual nuclei. To this end, we went on to prepare a series of isotope-labeled 4-OB•-containing reaction mixtures using different isotopologues of Tyr (Figure S4) and employed ENDOR spectroscopy to probe the hyperfine couplings of the magnetic nuclei (Figure 4).

We first measured the hyperfine couplings of all the ^1H atoms in 4-OB•. The ^1H Davies ENDOR spectrum of natural abundance (N.A.) 4-OB• collected at g = 2.004 is shown in Figure 4A (black trace) and Figure S5. The spectrum is centered at the $\nu_N(^1H)$ of 51.5 MHz. The outer region of the spectrum contains two obvious sets of ^1H ENDOR signals that are just separated from each other. Because of the small g-anisotropy, there is no orientation selection in the ENDOR spectra of 4-OB•, so that the spectra reveal the entire A tensor as seen from the classic "Pake pattern" in the figures. The ENDOR signal with larger ^1H hyperfine coupling, arising from the two benzyl ^1H atoms, has weak signal intensity due to its breadth. This ^1H hyperfine tensor is simulated with A ^1H = [66, 20, 41] MHz (red trace, Figure 4A). The ENDOR signal with smaller ^1H hyperfine coupling, arising from ring-2,6-$^1H_2$, is also nicely resolved in the narrower scan of the same sample and is simulated with A ^1H = [18.2, 7.0, 14.9] MHz (red trace, Figure 4B). The ENDOR signal of the remaining group of ^1H, ring-3,5-$^1H_2$, is buried in the central region and is overlapped with the signals arising from the remote/backbone and solvent ^1H with small hyperfine couplings. To extract this ^1H ENDOR signal, we used [ring-3,5-D_2]-Tyr to generate the corresponding isotopologue of 4-OB• (Figure 4C). The Davies ENDOR spectrum collected from this sample (blue trace) is overlapped with that of N.A. 4-OB• (black trace), and the difference spectra reveal the ENDOR signal arising from ring-3,5-$^1H_2$ (green trace), which is simulated with A ^1H = [5.3, 1.5, 3.8] MHz (red trace). Notably, the ^1H ENDOR lineshape is significantly distorted due to the suppression effect of Davies ENDOR, as A is close to zero. This ENDOR lineshape can be reproduced in spectral simulation using an intensity factor to account for the suppression effect (see the Experimental Details and sample script in the Supporting Information).[41]

To validate the assignments of ^1H ENDOR signals and to determine the hyperfine tensors more accurately, we prepared a series of ^2H-substituted 4-OB• and recorded the corresponding ^2H ENDOR spectra. The Davies ENDOR spectrum of [benzyl-D_2]-4-OB• is shown in Figure 5A (black trace) and

https://doi.org/10.1021/acs.biochem.1c00619
Biochemistry 2022, 61, 107−116

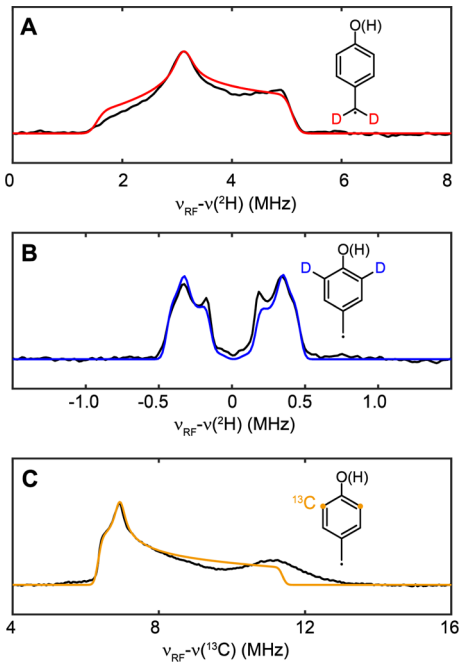

Figure 5. (A) Q-band Davies ^{2}H ENDOR spectra of [benzyl-D_2]-4-OB$^\bullet$. (B) Q-band Mims ^{2}H ENDOR spectra of [ring-3,5-D_2]-4-OB$^\bullet$. (C) Q-band ^{13}C Davies ENDOR spectra of [ring-3,5-$^{13}C_2$]-4-OB$^\bullet$. Black traces are experimental data, and color traces are simulations of ^{2}H and ^{13}C hyperfine coupling: (A) A ^{2}H = [10.2, 3.1, 6.3] MHz; (B) A ^{2}H = [0.23, 0.81, 0.60] MHz; and (C) A ^{13}C = [22.8, 12.7, 13.9] MHz. Conditions for Davies ENDOR (A,C) are the same as Figure 4. Conditions for Mims ENDOR (B): τ = 300 ns.

simulated with A ^{2}H = [10.2, 3.1, 6.3] MHz (red trace), which agrees well with the ^{1}H hyperfine coupling after scaling by the nuclear gyromagnetic ratio of ^{1}H and ^{2}H (g_N ^{1}H/g_N ^{2}H = 6.51). Here, only the ν_+ branch of the ENDOR signal is shown since ν_- is small and the ENDOR response in the low-RF range is weak and obscured. Again, the Davies ENDOR suppression effect also affects the ENDOR lineshape, and the intensity of features with small A is diminished. For the ring-3,5-D_2, the Mims ENDOR technique was applied because of the small ^{2}H hyperfine coupling (Figure 5B), and the ENDOR spectrum is centered at a ν_N(^{2}H) of 7.91 MHz. The spectral simulation used A ^{2}H = [0.23, 0.81, 0.60] MHz, consistent with the corresponding ^{1}H hyperfine parameters extracted from the difference spectrum shown in Figure 4C. In addition, to reproduce the lineshape in Figure 5B, a small ^{2}H nuclear quadrupole interaction (P ∼ [−0.05, −0.05, 0.1] MHz) is included in the simulation.

To probe the spin distribution on the carbon atoms, we generated the ^{13}C isotopologues of 4-OB$^\bullet$. Shown in Figure 5C is the Davies ENDOR spectrum of [ring-3,5-$^{13}C_2$]-4-OB$^\bullet$, simulated with A ^{13}C = [22.8, 12.7, 13.9] MHz. Here, again, only the ν_+ branch of the ENDOR signal is shown since A is close to 2ν_N (^{13}C), 13.0 MHz, so that the ν_- branch is weak and not observed. We also generated 4-OB$^\bullet$ isotopologues using [ring-4-^{13}C]-Tyr and [benzyl-^{13}C]-Tyr. However, their ^{13}C hyperfine couplings are largely dipolar and thus do not give any detectable ENDOR signals.

Using the pulse ENDOR-derived ^{1}H and ^{13}C hyperfine parameters, we were able to reproduce the complex lineshape of the Q-band EPR spectra of N.A. 4-OB$^\bullet$ and the ^{13}C-substituted isotopologues with high precision (Figures 3A and S6), which further substantiates the hyperfine values extracted from the ENDOR experiments. In the cases of [ring-4-^{13}C]-4-OB$^\bullet$ and [β-^{13}C]-4-OB$^\bullet$, only the largest principal A values, A_3, are determined from the spectral simulations. The hyperfine parameters used in the simulation of EPR and ENDOR spectra of various 4-OB$^\bullet$ are summarized in Table 1.

Table 1. Summary of ^{1}H, ^{2}H, and ^{13}C Hyperfine Parameters Used in the Simulation of EPR/ENDOR Spectra of 4-OB$^\bullet$

nuclei	A (MHz)	Euler angle (deg)
benzyl-^{1}H	[66, 20, 41]	[33, 5, 0]
ring-2,6-^{1}H	[18.2, 7.0, 14.9]	[31, 5, 0]
ring-3,5-^{1}H	[5.3, 1.5, 3.8]	[30, 0, 0]
exchangeable ^{1}H	[3.5, 1.6, −7.2][a]	[30, 5, 0]
benzyl-^{2}H	[10.2, 3.1, 6.3]	[33, 5, 0]
ring-3,5-^{2}H	[0.23, 0.81, 0.60]	[30, 0, 0]
benzyl-^{13}C	[∼, ∼, 160][b]	
ring-3,5-^{13}C	[22.8, 12.7, 13.9]	[20, 0, 0]
ring-4-^{13}C	[∼, ∼, 50][b]	

[a]Simulated as one effective ^{1}H. [b]A_1 and A_2 are small and not determined.

The phenol in p-cresol (pK_a = 10.3) or Tyr (pK_a = 10.98) is generally expected to be protonated under catalytic conditions; however, in the 4-OB$^\bullet$, which has one less H-atom compared to p-cresol, the deprotonated form could be stabilized by resonating with the ketyl-like 4-benzoquinone methide radical anion (Scheme 1A). To probe the protonation state of the phenolic hydroxyl and other exchangeable hydrogens in the vicinity of 4-OB$^\bullet$, we compared the ^{1}H ENDOR spectra of the reaction mixture prepared in H_2O and D_2O buffer. As shown in Figure 6A, the difference spectrum shows ENDOR signals predominantly at the central region, which can be effectively simulated with A ^{1}H = [3.5, 1.6, −7.2] MHz. The magnitude of this coupling thus supports that an exchangeable proton(s) is present near the spin center. However, it should be noted that this does not necessarily prove the presence of a protonated phenolic hydroxyl because the hydroxyl groups from protein residues that form hydrogen bonds to the phenolic oxygen could give rise to ^{1}H couplings of similar magnitude, as demonstrated from the DFT calculations (*vide infra*). Indeed, the modeled structures of 4-OB$^\bullet{}_H$ or 4-OB$^\bullet$ docked in the protein pocket, obtained from our recent QM/MM study,[24] indicate that several polar residues and a water molecule are within the range of polar contact and form a hydrogen bonding network (Figure 6B,C).

Although the protonation state of 4-OB$^\bullet$ is not reflected in the ENDOR results directly, it does affect the patterns of the hydrogen bonding networks near the phenol hydroxyl, which has been shown to be influential to the EPR and ENDOR parameters of organic radicals. DFT calculations have proven to be useful in discriminating between the possible structures in such systems.[66,67] Given the rich EPR data—in terms of high-resolution g tensor and a collection of different A values—gleaned from our EPR and ENDOR experiments, we sought to perform DFT calculations of different 4-OB$^\bullet$ models to help clarify this issue (Figure S7 and Table 2). We first considered the simplest 4-OB$^\bullet$ models in two different protonation states (4-OB$^\bullet{}_O$ and 4-OB$^\bullet{}_{OH}$). The calculated g-values and A values of both models show relatively large discrepancies to the experimental values. In general, the 4-OB$^\bullet{}_O$ model predicts hyperfine values too small, whereas the

https://doi.org/10.1021/acs.biochem.1c00619
Biochemistry 2022, 61, 107−116

Scheme 1. (A) Resonance Structures of 4-OB• between the Benzyl Radical and the Ketyl Radicals and (B) Formation of 4-OB• in HpdB via a Kolbe-Type Decarboxylation, which is a Concerted Proton-Coupled Electron Transfer Reaction, as Opposed to H Atom Abstraction in HydG

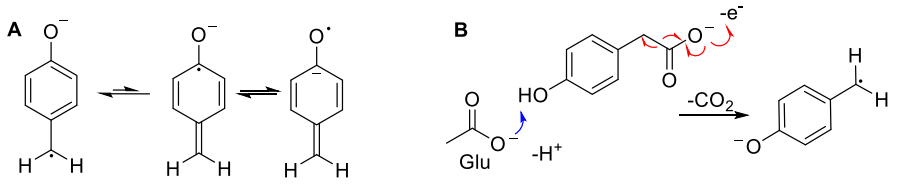

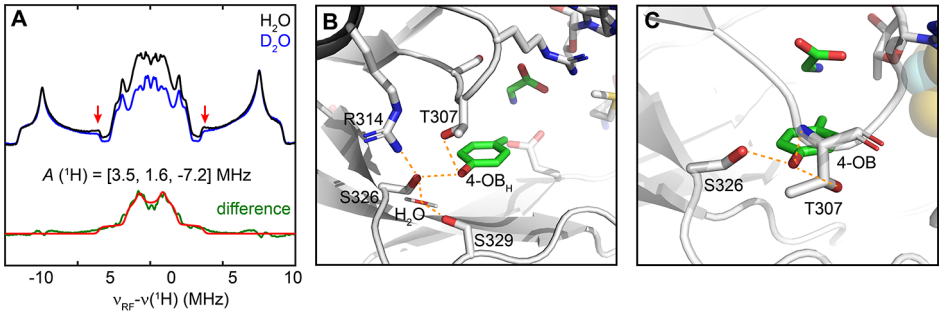

Figure 6. (A) Comparison of the ^{1}H ENDOR spectra between 4-OB• generated in H_2O and D_2O. The largest *A* value in the difference spectrum is indicated by the arrows. The difference spectrum is simulated with *A* ^{1}H = [3.5, 1.6, −7.2] MHz. (B) QM/MM-modeled structure of 4-OB•$_H$ (in green) poised in the protein pocket showing polar contacts with nearby residues. (C) QM/MM-modeled structure of 4-OB•. Orange dot lines indicate the polar contacts between the phenolic hydroxyl and nearby atoms (hydrogen atoms are omitted).

Table 2. Comparison of Experimental and DFT-Predicted EPR/ENDOR Parameters of Different 4-OB• Models[a]

model	*g*	*β*-^{1}H	2,6-^{1}H	3,5-^{1}H
Experiment	2.00(37, 36, 26)	[66, 20, 41]	[7, 18, 15]	[1.6, 5.3, 3.9]
4-OB•$_O$	2.00(41, 37, 22)	[62, 16, 40]	[4, 15, 13]	[−0.8, 1.6, −2.6]
4-OB•$_{OH}$	2.00(32, 29, 22)	[75, 20, 50]	[7, 22, 18]	[3.2, 8.6, 4.3]
4-OB•$_O$-1	2.00(35, 31, 22)	[67, 16, 42]	[5, 18, 15]	[0.8, 4.7, 2.9]
4-OB•$_{OH}$-1	2.00(30, 28, 23)	[72, 17, 47]	[8, 21, 18]	[3.6, 8.7, 4.6]
4-OB•$_O$-DHG	2.00(43, 30, 17)	[64, 16, 41]	[5, 18, 15]	[0.9, 4.6, 2.8]
4-OB•$_{OH}$-DHG	2.00(32, 29, 18)	[73, 17, 48]	[9, 21, 18]	[3.7, 8.8, 4.6]
	3,5-^{13}C	*β*-^{13}C	4-^{13}C	exchangeable ^{1}H[b]
Experiment	[23, 13, 14]	[∼, ∼, 160]	[∼, ∼, 50]	[∼, ∼7]
4-OB•$_O$	[−10, −9, −10]	[7, 8, 139]	[−5, −8, 20]	
4-OB•$_{OH}$	[35, 13, 15]	[10, 11, 169]	[4, 5, 62]	[4, −6, −8]
4-OB•$_O$-1	[19, 10, 11]	[16, 16, 161]	[−1, −3, 33]	[−2, −3, 5]
4-OB•$_{OH}$-1	[34, 13, 14]	[33, 34, 195]	[4, 5, 58]	[0, −2, 9]
4-OB•$_O$-DHG	[20, 10, 10]	[18, 18, 157]	[−2, −3, 31]	[1, −2, −6]
4-OB•$_{OH}$-DHG	[34, 13, 15]	[32, 33, 191]	[4, 5, 58]	[0, −1, 9]

[a]All hyperfine values are in MHz. [b]Only the largest one is listed.

4-OB•$_{OH}$ model predicts hyperfine values a bit too large. We then constructed two larger models (4-OB•$_O$-1 and 4-OB•$_{OH}$-1) based on the QM/MM-predicted structures (Figure 6B,C) to include the nearby residues and water that have the closest polar contact to 4-OB•. The 4-OB•$_O$-1 model appears to agree quite well with the experimental results overall except for the 4-^{13}C hyperfine coupling, whereas a bigger model of the protonated 4-OB•$_{OH}$-1 does not improve the prediction accuracy significantly.

It is shown from the QM/MM models that the DHG fragment is situated near the benzyl end of 4-OB•, but there is not any direct electrostatic interaction between them. To evaluate the effect of DHG on the computational results, we further constructed two larger models, 4-OB•$_O$-DHG and 4-OB•$_{OH}$-DHG, to include the DHG fragment along with more residues that are linked to DHG through polar interactions (Figure S7). In both cases, the extended networks form dome-like frameworks surrounding 4-OB•, which should suffice to account for the primary protein environment of 4-OB•. As shown in Table 1, these two models give similar predicted hyperfine couplings compared to 4-OB•$_O$-1 and 4-OB•$_{OH}$-1, respectively, indicating that the contribution of the DHG fragment to the electronic structure of 4-OB• is not significant and that even bigger models are probably not necessary. Overall, the computed *g* and *A* values of the deprotonated models 4-OB•$_O$-1 and 4-OB•$_O$-DHG match the experimental results quite well, except for the hyperfine coupling of 4-^{13}C, which is better produced in the protonated models. In short, the survey of various DFT models supports that the 4-OB• trapped in the HydG reaction adopts the deprotonated state embedded into the hydrogen bonding network of the protein pocket.

https://doi.org/10.1021/acs.biochem.1c00619
Biochemistry 2022, 61, 107−116

Since the formation of 4-OB$^{\bullet}$ has been investigated by mutagenesis and computational studies in the glycyl radical enzyme 4-hydroxyphenylacetate decarboxylase (HpdB) which is involved in the fermentative production of *p*-cresol from tyrosine in *Clostridia*,[32,33] it is interesting to compare it with HydG. In the latter case, 4-OB$^{\bullet}$ is generated from a Kolbe-type decarboxylation of the 4-hydroxyphenylacetate radical anion facilitated by the parallel orbital alignment of the aromatic system, and a radical anion form of 4-OB$^{\bullet}$ has been proposed in this mechanism. The X-ray structure of HpdB and QM/MM-optimized geometry of the substrate-bound state indicate that a glutamate residue is in close proximity to the substrate phenolic hydroxyl group. This glutamate has been proposed to be crucial as a proton donor/acceptor during substrate activation and decarboxylation. In the case of HydG, a similar glutamate or aspartate is not identified near the hydroxyl side of the pocket. It is possible that the proton is transferred through the hydrogen bonding relay to nearby water molecules. This difference may be attributed to the fact that in HpdB, the glycyl radical abstracts only one electron from the substrate (4-hydroxyphenylacetate anion) at the carboxylate group; therefore, the deprotonation at the phenolic hydroxyl group, assisted by a glutamate residue, is necessary to facilitate a concerted proton-coupled electron transfer process, which effectively abstracts an electron and a proton, that is, *de facto* an H atom from the substrate (Scheme 1B). In contrast, in the case of HydG, the 5′-dAdo radical directly abstracts an H atom from tyrosine to initiate the radical bond scission, and deprotonation of the substrate at the initial step is not required.

Our results imply that the pK_a of the 4-oxidobenzyl radical is lower than the pH of the buffer (pH = 8.0) used in the assay. We attempted to calculate the pK_a of the 4-hydroxylbenzyl radical using the calculated pK_a of *p*-cresol as a reference (experimental pK_a = 10.3 for *p*-cresol). The computed pK_a for free 4-OB$^{\bullet}{}_H$ and *p*-cresol is 8.6 and 9.2, respectively (Table S2). The lowered pK_a for 4-OB$^{\bullet}{}_H$ compared to that of *p*-cresol is consistent with our analysis. Moreover, when poised in a protein pocket such as the models used for DFT calculations, the pK_a of 4-OB$^{\bullet}{}_H$ is further decreased to ∼4. While caution must be used to apply these computed pK_a values, these results are in support of a deprotonated form of 4-OB$^{\bullet}$ in HydG, consistent with the EPR and DFT results discussed above.

CONCLUSIONS

Our biochemical and EPR spectroscopic studies together with quantum chemical calculations reveal that the 4-OB$^{\bullet}$ intermediate in HydG catalysis is accumulated in HydG variants lacking the fifth Fe in the auxiliary Fe−S cluster, supporting a role of 4-OB$^{\bullet}$ in the catalytic pathway to cleave the DHG fragment into CO and CN$^-$ ligands relevant to this Fe site. This observation also provided us the opportunity to investigate the electronic structure of 4-OB$^{\bullet}$ in greater detail using advanced paramagnetic resonance techniques. Specifically, we determined the *g*-tensor of 4-OB$^{\bullet}$ with 130 GHz EPR and the ^{1}H and ^{13}C hyperfine couplings in a suite of 4-OB$^{\bullet}$ isotopologues by 34 GHz ENDOR spectroscopy, all of which allowed us to reproduce the complex EPR lineshapes of these species. In addition, DFT calculations of the hyperfine couplings of 4-OB$^{\bullet}$ in different protonation states in comparison with experiment led us to propose a radical anion configuration of 4-OB$^{\bullet}$ in the HydG pocket, which helps finalize the reaction mechanism of HydG and provides a method to clarify similar issues in other enzyme systems.

ASSOCIATED CONTENT

Supporting Information

The Supporting Information is available free of charge at https://pubs.acs.org/doi/10.1021/acs.biochem.1c00619.

Additional EPR spectra, structure of DFT models, and additional calculation results (PDF)

Accession Codes

Shewanella *oneidensis* HydG, *Shewanella oneidensis* HydG. NCBI accession ID: ADK73964.1, UniProt ID: Q8EAH9.

AUTHOR INFORMATION

Corresponding Author

R. David Britt − *Department of Chemistry, University of California Davis, Davis, California 95616, United States;* orcid.org/0000-0003-0889-8436; Email: rdbritt@ucdavis.edu

Authors

Guodong Rao − *Department of Chemistry, University of California Davis, Davis, California 95616, United States;* orcid.org/0000-0001-8043-3436

Nanhao Chen − *Department of Chemistry, University of California Davis, Davis, California 95616, United States*

David A. Marchiori − *Department of Chemistry, University of California Davis, Davis, California 95616, United States;* orcid.org/0000-0001-9738-3674

Lee-Ping Wang − *Department of Chemistry, University of California Davis, Davis, California 95616, United States;* orcid.org/0000-0003-3072-9946

Complete contact information is available at: https://pubs.acs.org/10.1021/acs.biochem.1c00619

Notes

The authors declare no competing financial interest.

ACKNOWLEDGMENTS

This work is funded by the National Health of Institutes (NIH 1R35GM126961 to R.D.B.). N.C. and L.P.W. acknowledge funding support from the Army Research Office, award number W911NF-17-1-0434.

REFERENCES

(1) Broderick, J. B.; Duffus, B. R.; Duschene, K. S.; Shepard, E. M. Radical S-adenosylmethionine enzymes. *Chem. Rev.* **2014**, *114*, 4229−4317.

(2) Nicolet, Y. Structure−function relationships of radical SAM enzymes. *Nat. Catal.* **2020**, *3*, 337−350.

(3) Horitani, M.; Shisler, K.; Broderick, W. E.; Hutcheson, R. U.; Duschene, K. S.; Marts, A. R.; Hoffman, B. M.; Broderick, J. B. Radical SAM catalysis via an organometallic intermediate with an Fe-[5′-C]-deoxyadenosyl bond. *Science* **2016**, *352*, 822−825.

(4) Byer, A. S.; Yang, H.; McDaniel, E. C.; Kathiresan, V.; Impano, S.; Pagnier, A.; Watts, H.; Denler, C.; Vagstad, A. L.; Piel, J.; Duschene, K. S.; Shepard, E. M.; Shields, T. P.; Scott, L. G.; Lilla, E. A.; Yokoyama, K.; Broderick, W. E.; Hoffman, B. M.; Broderick, J. B. Paradigm Shift for Radical S-Adenosyl-l-methionine Reactions: The Organometallic Intermediate Omega Is Central to Catalysis. *J. Am. Chem. Soc.* **2018**, *140*, 8634−8638.

(5) Yang, H.; McDaniel, E. C.; Impano, S.; Byer, A. S.; Jodts, R. J.; Yokoyama, K.; Broderick, W. E.; Broderick, J. B.; Hoffman, B. M. The

Elusive 5'-Deoxyadenosyl Radical: Captured and Characterized by Electron Paramagnetic Resonance and Electron Nuclear Double Resonance Spectroscopies. *J. Am. Chem. Soc.* **2019**, *141*, 12139−12146.
(6) Sayler, R. I.; Stich, T. A.; Joshi, S.; Cooper, N.; Shaw, J. T.; Begley, T. P.; Tantillo, D. J.; Britt, R. D. Trapping and Electron Paramagnetic Resonance Characterization of the 5'dAdo(*) Radical in a Radical S-Adenosyl Methionine Enzyme Reaction with a Non-Native Substrate. *ACS Cent. Sci.* **2019**, *5*, 1777−1785.
(7) Pagnier, A.; Yang, H.; Jodts, R. J.; James, C. D.; Shepard, E. M.; Impano, S.; Broderick, W. E.; Hoffman, B. M.; Broderick, J. B. Radical SAM Enzyme Spore Photoproduct Lyase: Properties of the Omega Organometallic Intermediate and Identification of Stable Protein Radicals Formed during Substrate-Free Turnover. *J. Am. Chem. Soc.* **2020**, *142*, 18652−18660.
(8) Kuchenreuther, J. M.; Myers, W. K.; Stich, T. A.; George, S. J.; Nejatyjahromy, Y.; Swartz, J. R.; Britt, R. D. A radical intermediate in tyrosine scission to the CO and CN^- ligands of FeFe hydrogenase. *Science* **2013**, *342*, 472−475.
(9) Tao, L.; Stich, T. A.; Fugate, C. J.; Jarrett, J. T.; Britt, R. D. EPR-derived structure of a paramagnetic intermediate generated by biotin synthase BioB. *J. Am. Chem. Soc.* **2018**, *140*, 12947−12963.
(10) Sicoli, G.; Mouesca, J.-M.; Zeppieri, L.; Amara, P.; Martin, L.; Barra, A.-L.; Fontecilla-Camps, J. C.; Gambarelli, S.; Nicolet, Y. Fine-tuning of a radical-based reaction by radical S-adenosyl-L-methionine tryptophan lyase. *Science* **2016**, *351*, 1320−1323.
(11) Horitani, M.; Byer, A. S.; Shisler, K. A.; Chandra, T.; Broderick, J. B.; Hoffman, B. M. Why Nature Uses Radical SAM Enzymes so Widely: Electron Nuclear Double Resonance Studies of Lysine 2,3-Aminomutase Show the 5'-dAdo* "Free Radical" Is Never Free. *J. Am. Chem. Soc.* **2015**, *137*, 7111−7121.
(12) Fu, B.; Balskus, E. P. Discovery of C-C bond-forming and bond-breaking radical enzymes: enabling transformations for metabolic engineering. *Curr. Opin. Biotechnol.* **2020**, *65*, 94−101.
(13) Balo, A. R.; Caruso, A.; Tao, L.; Tantillo, D. J.; Seyedsayamdost, M. R.; Britt, R. D. Trapping a cross-linked lysine-tryptophan radical in the catalytic cycle of the radical SAM enzyme SuiB. *Proc. Natl. Acad. Sci. U.S.A.* **2021**, *118*, No. e2101571118.
(14) Britt, R. D.; Rao, G.; Tao, L. Bioassembly of complex iron−sulfur enzymes: hydrogenases and nitrogenases. *Nat. Rev. Chem.* **2020**, *4*, 542−549.
(15) Lubitz, W.; Ogata, H.; Rüdiger, O.; Reijerse, E. Hydrogenases. *Chem. Rev.* **2014**, *114*, 4081−4148.
(16) Britt, R. D.; Rao, G.; Tao, L. Biosynthesis of the catalytic H-cluster of [FeFe] hydrogenase: the roles of the Fe−S maturase proteins HydE, HydF, and HydG. *Chem. Sci.* **2020**, *11*, 10313−10323.
(17) Shepard, E. M.; Mus, F.; Betz, J. N.; Byer, A. S.; Duffus, B. R.; Peters, J. W.; Broderick, J. B. [FeFe]-hydrogenase maturation. *Biochemistry* **2014**, *53*, 4090−4104.
(18) Peters, J. W.; Schut, G. J.; Boyd, E. S.; Mulder, D. W.; Shepard, E. M.; Broderick, J. B.; King, P. W.; Adams, M. W. W. [FeFe]- and [NiFe]-hydrogenase diversity, mechanism, and maturation. *Biochim. Biophys. Acta* **2015**, *1853*, 1350−1369.
(19) Kuchenreuther, J. M.; Myers, W. K.; Suess, D. L. M.; Stich, T. A.; Pelmenschikov, V.; Shiigi, S. A.; Cramer, S. P.; Swartz, J. R.; Britt, R. D.; George, S. J. The HydG enzyme generates an $Fe(CO)_2(CN)$ synthon in assembly of the FeFe hydrogenase H-cluster. *Science* **2014**, *343*, 424−427.
(20) Dinis, P.; Suess, D. L. M.; Fox, S. J.; Harmer, J. E.; Driesener, R. C.; De La Paz, L.; Swartz, J. R.; Essex, J. W.; Britt, R. D.; Roach, P. L. X-ray crystallographic and EPR spectroscopic analysis of HydG, a maturase in [FeFe]-hydrogenase H-cluster assembly. *Proc. Natl. Acad. Sci. U.S.A.* **2015**, *112*, 1362−1367.
(21) Nicolet, Y.; Pagnier, A.; Zeppieri, L.; Martin, L.; Amara, P.; Fontecilla-Camps, J. C. Crystal structure of HydG from *Carboxydothermus hydrogenoformans*: a trifunctional [FeFe]-hydrogenase maturase. *ChemBioChem* **2015**, *16*, 397−402.
(22) Tao, L.; Pattenaude, S. A.; Joshi, S.; Begley, T. P.; Rauchfuss, T. B.; Britt, R. D. Radical SAM Enzyme HydE Generates Adenosylated Fe(I) Intermediates En Route to the [FeFe]-Hydrogenase Catalytic H-Cluster. *J. Am. Chem. Soc.* **2020**, *142*, 10841−10848.
(23) Rohac, R.; Martin, L.; Liu, L.; Basu, D.; Tao, L.; Britt, R. D.; Rauchfuss, T. B.; Nicolet, Y. Crystal Structure of the [FeFe]-Hydrogenase Maturase HydE Bound to Complex-B. *J. Am. Chem. Soc.* **2021**, *143*, 8499−8508.
(24) Chen, N.; Rao, G.; Britt, R. D.; Wang, L.-P. Quantum Chemical Study of a Radical Relay Mechanism for the HydG-Catalyzed Synthesis of a Fe(II)(CO)2(CN)cysteine Precursor to the H-Cluster of [FeFe] Hydrogenase. *Biochemistry* **2021**, *60*, 3016−3026.
(25) Rao, G.; Tao, L.; Suess, D. L. M.; Britt, R. D. A [4Fe-4S]-Fe(CO)(CN)-L-cysteine intermediate is the first organometallic precursor in [FeFe] hydrogenase H-cluster bioassembly. *Nat. Chem.* **2018**, *10*, 555−560.
(26) Suess, D. L. M.; Bürstel, I.; De La Paz, L.; Kuchenreuther, J. M.; Pham, C. C.; Cramer, S. P.; Swartz, J. R.; Britt, R. D. Cysteine as a ligand platform in the biosynthesis of the FeFe hydrogenase H cluster. *Proc. Natl. Acad. Sci. U.S.A.* **2015**, *112*, 11455−11460.
(27) Suess, D. L. M.; Pham, C. C.; Bürstel, I.; Swartz, J. R.; Cramer, S. P.; Britt, R. D. The radical SAM enzyme HydG requires cysteine and a dangler iron for generating an organometallic precursor to the [FeFe]-hydrogenase H-cluster. *J. Am. Chem. Soc.* **2016**, *138*, 1146−1149.
(28) Yang, H.; Impano, S.; Shepard, E. M.; James, C. D.; Broderick, W. E.; Broderick, J. B.; Hoffman, B. M. Photoinduced Electron Transfer in a Radical SAM Enzyme Generates an S-Adenosylmethionine Derived Methyl Radical. *J. Am. Chem. Soc.* **2019**, *141*, 16117−16124.
(29) Impano, S.; Yang, H.; Shepard, E. M.; Swimley, R.; Pagnier, A.; Broderick, W. E.; Hoffman, B. M.; Broderick, J. B. S-Adenosyl-l-ethionine is a Catalytically Competent Analog of S-Adenosyl-l-methione (SAM) in the Radical SAM Enzyme HydG. *Angew. Chem., Int. Ed. Engl.* **2021**, *60*, 4666−4672.
(30) Pagnier, A.; Martin, L.; Zeppieri, L.; Nicolet, Y.; Fontecilla-Camps, J. C. CO and CN^- syntheses by [FeFe]-hydrogenase maturase HydG are catalytically differentiated events. *Proc. Natl. Acad. Sci. U.S.A.* **2016**, *113*, 104−109.
(31) Wu, Y.; Wu, R.; Mandalapu, D.; Ji, X.; Chen, T.; Ding, W.; Zhang, Q. Radical SAM-dependent adenosylation catalyzed by l-tyrosine lyases. *Org. Biomol. Chem.* **2019**, *17*, 1809−1812.
(32) Martins, B. M.; Blaser, M.; Feliks, M.; Ullmann, G. M.; Buckel, W.; Selmer, T. Structural basis for a Kolbe-type decarboxylation catalyzed by a glycyl radical enzyme. *J. Am. Chem. Soc.* **2011**, *133*, 14666−14674.
(33) Feliks, M.; Martins, B. M.; Ullmann, G. M. Catalytic mechanism of the glycyl radical enzyme 4-hydroxyphenylacetate decarboxylase from continuum electrostatic and QC/MM calculations. *J. Am. Chem. Soc.* **2013**, *135*, 14574−14585.
(34) Rittle, J. The Key Intermediate in Radical S-Adenosylmethionine Catalysis: Caught in the Act. *ACS Cent. Sci.* **2019**, *5*, 1741−1743.
(35) Calvo, R.; Abresch, E. C.; Bittl, R.; Feher, G.; Hofbauer, W.; Isaacson, R. A.; Lubitz, W.; Okamura, M. Y.; Paddock, M. L. EPR study of the molecular and electronic structure of the semiquinone biradical $Q_a^-\bullet Q_b^-\bullet$ in photosynthetic reaction centers from *Rhodobacter sphaeroides*. *J. Am. Chem. Soc.* **2000**, *122*, 7327−7341.
(36) Oyala, P. H.; Ravichandran, K. R.; Funk, M. A.; Stucky, P. A.; Stich, T. A.; Drennan, C. L.; Britt, R. D.; Stubbe, J. Biophysical Characterization of Fluorotyrosine Probes Site-Specifically Incorporated into Enzymes: E. coli Ribonucleotide Reductase As an Example. *J. Am. Chem. Soc.* **2016**, *138*, 7951−7964.
(37) Epel, B.; Gromov, I.; Stoll, S.; Schweiger, A.; Goldfarb, D. Spectrometer manager: A versatile control software for pulse EPR spectrometers. *Concepts Magn. Reson., Part B* **2005**, *26B*, 36−45.
(38) Stoll, S.; Gunn, A.; Brynda, M.; Sughrue, W.; Kohler, A. C.; Ozarowski, A.; Fisher, A. J.; Lagarias, J. C.; Britt, R. D. Structure of the biliverdin radical intermediate in phycocyanobilin:ferredoxin oxidoreductase identified by high-field EPR and DFT. *J. Am. Chem. Soc.* **2009**, *131*, 1986−1995.

https://doi.org/10.1021/acs.biochem.1c00619
Biochemistry 2022, 61, 107−116

(39) Stoll, S.; Ozarowski, A.; Britt, R. D.; Angerhofer, A. Atomic hydrogen as high-precision field standard for high-field EPR. *J. Magn. Reson.* **2010**, *207*, 158−163.
(40) Stoll, S.; Schweiger, A. EasySpin, a comprehensive software package for spectral simulation and analysis in EPR. *J. Magn. Reson.* **2006**, *178*, 42−55.
(41) Doan, P. E.; Lees, N. S.; Shanmugam, M.; Hoffman, B. M. Simulating suppression effects in Pulsed ENDOR, and the 'hole in the middle' of Mims and Davies ENDOR Spectra. *Appl. Magn. Reson.* **2010**, *37*, 763−779.
(42) Schweiger, A.; Jeschke, G. *Principles of Pulse Electron Paramagnetic Resonance*; Oxford University Press: USA, 2001.
(43) Nicolet, Y.; Zeppieri, L.; Amara, P.; Fontecilla-Camps, J. C. Crystal structure of tryptophan lyase (NosL): evidence for radical formation at the amino group of tryptophan. *Angew. Chem., Int. Ed. Engl.* **2014**, *53*, 11840−11844.
(44) Wang, L.-P.; McKiernan, K. A.; Gomes, J.; Beauchamp, K. A.; Head-Gordon, T.; Rice, J. E.; Swope, W. C.; Martínez, T. J.; Pande, V. S. Building a More Predictive Protein Force Field: A Systematic and Reproducible Route to AMBER-FB15. *J. Phys. Chem. B* **2017**, *121*, 4023−4039.
(45) Chang, C. H.; Kim, K. Density Functional Theory Calculation of Bonding and Charge Parameters for Molecular Dynamics Studies on [FeFe] Hydrogenases. *J. Chem. Theory Comput.* **2009**, *5*, 1137−1145.
(46) Andersen, H. C. Molecular dynamics simulations at constant pressure and/or temperature. *J. Chem. Phys.* **1980**, *72*, 2384−2393.
(47) Shao, Y.; Gan, Z.; Epifanovsky, E.; Gilbert, A. T.; Wormit, M.; Kussmann, J.; Lange, A. W.; Behn, A.; Deng, J.; Feng, X.; et al. Advances in molecular quantum chemistry contained in the Q-Chem 4 program package. *Mol. Phys.* **2015**, *113*, 184−215.
(48) Zhou, Y.; Wang, S.; Li, Y.; Zhang, Y. Born−Oppenheimer ab initio QM/MM molecular dynamics simulations of enzyme reactions. *Methods Enzymol.* **2016**, *577*, 105−118.
(49) Salomon-Ferrer, R.; Case, D. A.; Walker, R. C. An overview of the Amber biomolecular simulation package. *Wiley Interdiscip. Rev.: Comput. Mol. Sci.* **2013**, *3*, 198−210.
(50) Neese, F. The ORCA program system. *Wiley Interdiscip. Rev.: Comput. Mol. Sci.* **2012**, *2*, 73−78.
(51) Becke, A. D. Density-functional exchange-energy approximation with correct asymptotic behavior. *Phys. Rev. A: Gen. Phys.* **1988**, *38*, 3098−3100.
(52) Lee, C.; Yang, W.; Parr, R. G. Development of the Colle-Salvetti correlation-energy formula into a functional of the electron density. *Phys. Rev. B: Condens. Matter Mater. Phys.* **1988**, *37*, 785−789.
(53) Becke, A. D. Density-functional thermochemistry. III. The role of exact exchange. *J. Chem. Phys.* **1993**, *98*, 5648−5652.
(54) Neese, F.; Wennmohs, F.; Hansen, A. Efficient and accurate local approximations to coupled-electron pair approaches: An attempt to revive the pair natural orbital method. *J. Chem. Phys.* **2009**, *130*, 114108.
(55) Staroverov, V. N.; Scuseria, G. E.; Tao, J.; Perdew, J. P. Comparative assessment of a new nonempirical density functional: Molecules and hydrogen-bonded complexes. *J. Chem. Phys.* **2003**, *119*, 12129−12137.
(56) Barone, V.; Cossi, M. Quantum calculation of molecular energies and energy gradients in solution by a conductor solvent model. *J. Phys. Chem. A* **1998**, *102*, 1995−2001.
(57) Grimme, S.; Ehrlich, S.; Goerigk, L. Effect of the damping function in dispersion corrected density functional theory. *J. Comput. Chem.* **2011**, *32*, 1456−1465.
(58) Barone, V. *Recent Advances in Density Functional Methods, Part I*; World Scientific Publ. Co.: Singapore, 1996.
(59) Schindler, M.; Kutzelnigg, W. Theory of magnetic susceptibilities and NMR chemical shifts in terms of localized quantities. II. Application to some simple molecules. *J. Chem. Phys.* **1982**, *76*, 1919−1933.
(60) Hedegård, E. D.; Kongsted, J.; Sauer, S. P. A. Optimized Basis Sets for Calculation of Electron Paramagnetic Resonance Hyperfine Coupling Constants: aug-cc-pVTZ-J for the 3d Atoms Sc−Zn. *J. Chem. Theory Comput.* **2011**, *7*, 4077−4087.
(61) Seritan, S.; Bannwarth, C.; Fales, B. S.; Hohenstein, E. G.; Kokkila-Schumacher, S. I. L.; Luehr, N.; Snyder, J. W., Jr.; Song, C.; Titov, A. V.; Ufimtsev, I. S.; Martínez, T. J. TeraChem: Accelerating electronic structure and ab initio molecular dynamics with graphical processing units. *J. Chem. Phys.* **2020**, *152*, 224110.
(62) Peintinger, M. F.; Oliveira, D. V.; Bredow, T. Consistent Gaussian basis sets of triple-zeta valence with polarization quality for solid-state calculations. *J. Comput. Chem.* **2013**, *34*, 451−459.
(63) Sproviero, E. M.; Gascón, J. A.; McEvoy, J. P.; Brudvig, G. W.; Batista, V. S. Quantum mechanics/molecular mechanics study of the catalytic cycle of water splitting in photosystem II. *J. Am. Chem. Soc.* **2008**, *130*, 3428−3442.
(64) Klamt, A. The COSMO and COSMO-RS solvation models. *Wiley Interdiscip. Rev.: Comput. Mol. Sci.* **2018**, *8*, No. e1338.
(65) Rao, G.; Alwan, K. B.; Blackburn, N. J.; Britt, R. D. Incorporation of Ni^{2+}, Co^{2+}, and Selenocysteine into the Auxiliary Fe-S Cluster of the Radical SAM Enzyme HydG. *Inorg. Chem.* **2019**, *58*, 12601−12608.
(66) Argirević, T.; Riplinger, C.; Stubbe, J.; Neese, F.; Bennati, M. ENDOR Spectroscopy and DFT Calculations: Evidence for the Hydrogen-Bond Network Within α2 in the PCET of E. coli Ribonucleotide Reductase. *J. Am. Chem. Soc.* **2012**, *134*, 17661−17670.
(67) Benisvy, L.; Bittl, R.; Bothe, E.; Garner, C. D.; McMaster, J.; Ross, S.; Teutloff, C.; Neese, F. Phenoxyl radicals hydrogen-bonded to imidazolium: analogues of tyrosyl D. of photosystem II: high-field EPR and DFT studies. *Angew. Chem., Int. Ed. Engl.* **2005**, *44*, 5314−5317.

https://doi.org/10.1021/acs.biochem.1c00619
Biochemistry 2022, 61, 107−116